




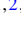


Evolution of the confined states in graphene nanobubbles

Zewen Wu ^{1,2,3,*}, Zhen Zhan ^{4,1}, Jose Angel Silva-Guillén ^{4,†}, Francisco Guinea ⁴,
Mikhail I. Katsnelson ³, and Shengjun Yuan ^{1,2,‡}

¹Key Laboratory of Artificial Micro- and Nano-structures of the Ministry of Education and School of Physics and Technology, Wuhan University, Wuhan 430072, China

²Wuhan Institute of Quantum Technology, Wuhan 430206, China

³Institute for Molecules and Materials, Radboud University, Heijendaalseweg 135, NL-6525 AJ Nijmegen, Netherlands

⁴IMDEA Nanoscience, C/ Faraday 9, 28049, Madrid, Spain



(Received 11 October 2023; revised 4 January 2024; accepted 13 February 2024; published 15 March 2024)

In this study, we use a full tight-binding model to explore the behavior of graphene nanobubbles between the interface of twisted bilayer graphene (TBG-1.05°), uncovering the simultaneous existence of confined states and pseudo-Landau level (pLL) states under minor strain conditions. We find that the energy separation of the confined states aligns with a linear N rule, while pLL states follow a typical \sqrt{N} rule. As the height of the bubble and the local strain escalate, the low-energy segment of the local density of states transforms from confined states to pLL states. Our findings establish that the effect of a perpendicular magnetic field can effectively distinguish between confined and pLLs. Our results offer a crucial stepping stone towards the strain-engineering of electronic states in graphene-based nanostructures.

DOI: [10.1103/PhysRevB.109.115420](https://doi.org/10.1103/PhysRevB.109.115420)

I. INTRODUCTION

Graphene, a single-layered structure of carbon atoms, has sparked significant interest across diverse scientific fields, from physics to biology, thanks to its unique electronic and structural properties [1]. These properties underpin a range of intriguing phenomena in condensed matter physics. Notably, the application of a perpendicular magnetic field to a graphene device results in the emergence of Landau levels (LLs) and the quantum Hall effect (QHE), with a formation of topologically protected zero-energy Landau level characteristic for massless Dirac fermions [1–3]. This observation has initiated the graphene boom. Among the latest exciting discoveries, recent experiments have unveiled superconductivity and correlated states in twisted bilayer graphene samples associated with the flat band formation [4–6].

The importance of graphene in the scientific community is substantial, paving the way for new research avenues such as straintronics, spintronics, valleytronics, and twistrionics. The strain has emerged as a potent tool to manipulate the electronic properties of two-dimensional (2D) materials, leading not only to innovative technological devices but also to exotic fundamental phenomena. For instance, strain-induced pseudomagnetic fields (PMFs) have been observed to generate LL-like peaks in strained graphene samples [1,7,8].

In standard experimental samples, graphene nanobubbles (GNBs) naturally occur due to a self-cleansing process that traps hydrocarbons between the substrate's top layer and the 2D material [9–12]. These bubbles, subject to high levels

of strain, can induce PMFs reaching up to 300 T [8]. Advances in experimental techniques, such as functional atomic force microscopy (AFM) and scanning tunneling microscopy (STM), now allow for the artificial control of GNB shape and size [13,14]. Moreover, recent studies have highlighted that bubbles created from van der Waals materials can function as tunable photoluminescence emitters when supported by different substrates [12].

Investigating the electronic structure of graphene nanobubbles is crucial for understanding strain-induced PMFs and their potential applications in topological materials, spintronics, photonics, and superconductivity. As such, a fundamental exploration of these nanostructures is vital for enhancing our understanding of future electronic devices and the behavior of samples under extremely high magnetic fields.

In this paper, we delve into a theoretical examination of the electronic properties of GNBs in twisted bilayer graphene (TBG), utilizing a full tight-binding (TB) model. By scrutinizing three distinct bubble shapes encountered in experimental samples [9,11,15–19], we reveal that the bubble's strain profile gives rise to two types of states: strain-induced confined states and pseudo-Landau level (pLL) states. This observation remains consistent across different bubble shapes, underlining the need to comprehend the interplay between strain and electronic properties in graphene nanobubbles.

II. PARABOLOID BUBBLE

In single-layer graphene experiments, prototypical bubbles often form due to the entrapment of gas or liquid between the graphene layer and the substrate. Typically, these bubbles assume a paraboloidal shape, as illustrated in the inset of Fig. 1(a) [11,20–22]. Recently, experimenters discovered the existence of nanobubbles at the interface of tiny-angle twisted

*zw.wu@whu.edu.cn

†josilgui@gmail.com

‡s.yuan@whu.edu.cn

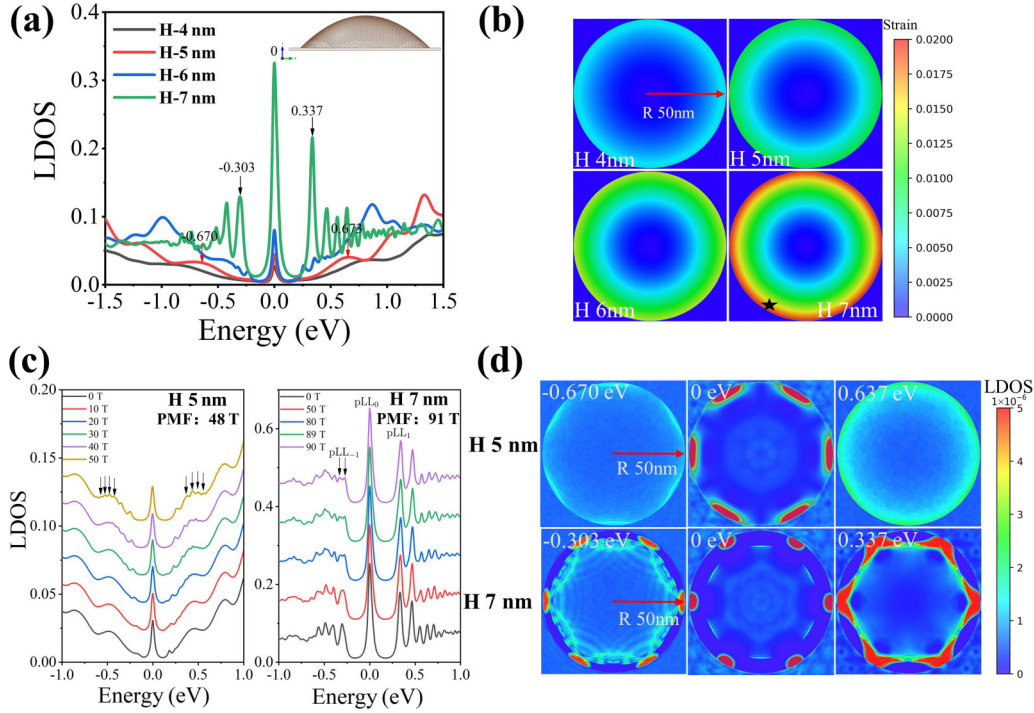


FIG. 1. (a) Evolution of the local density of states (LDOS) at a site situated at the distance $0.97R$ from the bubble center in relation to the height of the bubble, illustrated alongside a lateral view of a single parabolic bubble. (b) Strain profiles for the bubble portrayed in (a) at different heights, maintaining a fixed radius of 50 nm. (c) LDOS at the site situated at the distance $0.95R$ from the bubble center under an array of perpendicular real magnetic fields for single parabolic bubbles of heights 5 and 7 nm, respectively. (d) Quasi-eigenstates corresponding to the LDOS peaks depicted in (a).

bilayer graphene [10]. With the use of AFM or STM tips, researchers are now capable of generating these bubbles in graphene samples by applying various bias levels [9,13].

We decided to examine realistic bubbles with a radius of 50 nm and calculated their electronic properties for various height values. In our model, we only adjusted the z coordinates of the atoms by δz using a smooth bump function expressed as

$$\delta z = H \left(1 - \frac{(x - x_0)^2 + (y - y_0)^2}{R^2} \right), \quad (1)$$

Here H and R represent the height and radius of the bubble, respectively, and (x_0, y_0) indicates the central position of the bubble in the x - y plane.

The local strain can be determined using the distance of a carbon atom to its three nearest neighbors as follows:

$$\epsilon = \frac{d_1 + d_2 + d_3}{3d_0} - 1, \quad (2)$$

In this equation, d_0 is the carbon-carbon distance without deformation, while d_1, d_2, d_3 are the distances between the three nearest neighbors of a carbon atom. As demonstrated in Fig. 1(b), the maximum strain is situated around the bubble edge, independent of the height. A prominent feature of the bubbles formed in graphene is the emergence of pLLs due to the formation of strain-induced giant PMFs [8], these pLLs appear at the bubble edges [9]. Therefore it is only natural to look for these features in the bubbles that we are simulating. To do so, we calculate (see numerical methods in the Appendix A) the local density of states (LDOS) at a position

near the edge. As we look at the evolution of the features of the LDOS with varying bubble height in Fig. 1(a), we see several striking features. The first one is that, independently of the bubble height (hence of the strain), a zero energy peak appears in the spectrum. Moreover, this peak is enhanced when the height increases. A typical feature of the Landau levels that arise when graphene is under a real magnetic field is the appearance of a zero energy state [7,23]. Therefore a first approach to understand the origin of the satellite peaks would be fitting the satellite peaks to the well-known equation for the quantized Landau levels in the LDOS spectrum of strained graphene [1,7–9,23]:

$$E_n = \pm \sqrt{2e\hbar v_f^2 |N| |\mathbf{B}_S|} + E_{\text{Dirac}} \quad (3)$$

$$N = \dots - 2, -1, 0, 1, 2, \dots$$

With this in mind, and taking a closer look at the satellite peaks, we find two different kinds of behaviors. (i) If the bubble height is smaller than 5 nm the peaks are equally spaced and broad [Figs. 1(c) and 2(a)]. Moreover, these peaks shift towards the Fermi level and become slightly narrower. (ii) When the height of the bubble is increased further, very narrow peaks start emerging close to the Fermi level. Consequently, these two peaks must have different physical origins.

Indeed, the generalized peaks appear akin to the previously observed confined states manifested in graphene quantum dots [24]. The electrostatic potential which has the form [25,26]

$$V = 2g_1 \left(\frac{d_1 + d_2 + d_3}{3d_0} - 1 \right) = 2g_1 \epsilon. \quad (4)$$

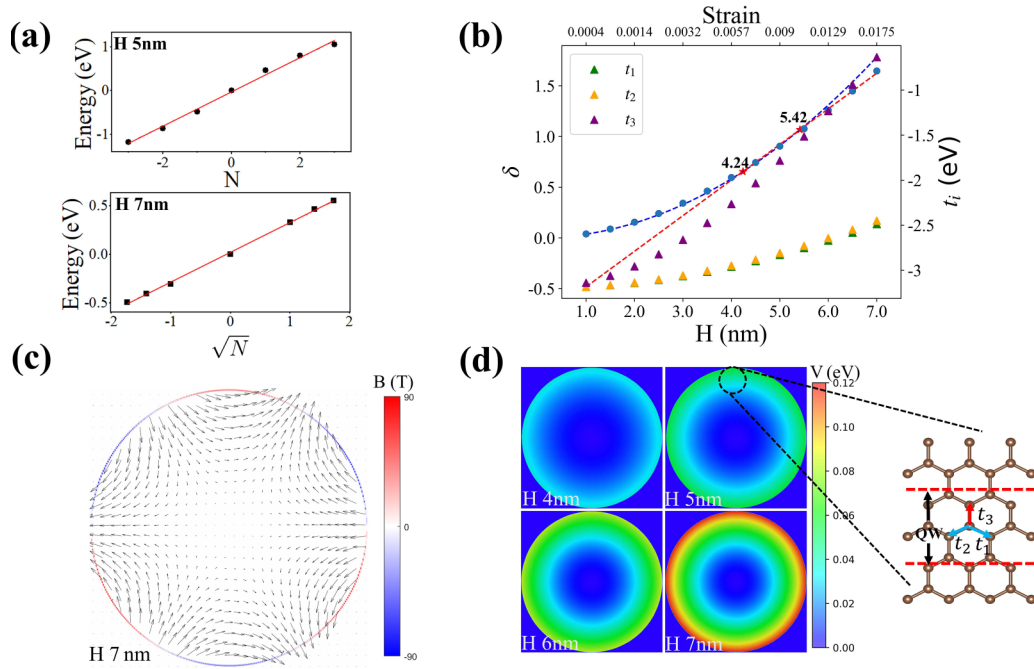


FIG. 2. (a) Fitted LDOS peaks at site $0.95R$ for bubble heights of 5 and 7 nm, respectively. (b) The defined hopping function, $\delta = \sqrt{\frac{1}{3} \sum_{i=1}^3 (t_i - t_0)^2}$, where t_i and t_0 represent the site's nearest neighbor hoppings with and without deformation, respectively, varies with bubble height at site $0.97R$. The blue dashed line corresponds to data fitted for bubble heights less than 5 nm, while the red line corresponds to data fitted for bubble heights greater than 5 nm. (c) The distribution of the angle-dependent PMF in a single paraboloid bubble with a height of 7 nm, the arrows denote the flow directions of the vector field. (d) A contour plot showing the deformation potential variation with bubble heights ranging from 4 to 7 nm. The zoomed-in section illustrates the formation of the strain-induced finite quantum well at the bubble's edge.

$g_1 \approx 4$ eV is the deformation potential for graphene depicted in Fig. 2(d) manifests an annular shape near the boundary of the bubble, indicative of a finite quantum well that localizes electrons. As illustrated in Fig. 2(d), the expansion of the bubble height engenders a broader equipotential region. Further augmentation of the height culminates in an enhanced potential; nevertheless, the electrostatic potential is relatively minute and can only localize either electrons or holes. Consequently, the confinement primarily emanates from the PMF inherent in the system [27]. The augmentation of the bubble height results in the formation of a one-dimensional (1D), annular finite quantum well, strengthening the PMF as depicted in Fig. 1(c), thereby deepening the potential induced by the nonuniform PMF. Significantly, the PMF localizes both electrons and holes, leading to the manifestation of confined states exhibiting an energy equal-spacing phenomenon [27]. This can be roughly approximated using the formula $\Delta E \approx \pi \hbar v_f / l$, wherein v_f denotes the Fermi velocity and l represents the width of the finite quantum well [27]. The fitting of the energies of confined states displayed in Fig. 2(a) provides further corroboration that these states are equally spaced within the energy spectrum [27].

We now center our attention on the other peaks that emerge when the bubble height is larger. As we have said before, these peaks are pLLs since they follow the quantized spectrum of the LDOS of strained graphene [1,7,28]. To further corroborate our findings, we have studied the quasideigenstates in real space for several peaks, which we show in Fig. 1(d). The central peak in the LDOS (H-5 nm) and (H-7 nm) are due to strain-induced pLLs [1,29] since both of them grow with

strain and show a clear angle-dependent distribution in real space. This is in line with experimental results [9,12]. As we can see, the confined states (top row of 1st and 3rd column of Fig. 1(d)) are continuously distributed around the edge of the bubble forming a ring, while the pLLs are localized at certain positions (bottom row of Fig. 1(d)). Interestingly, they show three-fold symmetry [9,12].

While STM techniques can be utilized to distinguish the differences between states observed in various bubbles, accurately measuring minor shifts in atomic positions can pose a significant challenge [14]. Intriguingly, an additional approach can be adopted, involving the application of a perpendicular magnetic field on the GNB. This method produces distinctive effects on the confined states and the pLLs [14,27,30].

The LDOS peaks of confined states undergo splitting at low fields while splitting the pLLs requires the application of a real magnetic field nearly equivalent to the strength of the PMF [14]. This effect can be calculated by adjusting the tight-binding parameters using Peierls substitution [31]. The results are displayed in Fig. 1(c).

Observably, in the case of a 5 nm high bubble, where only the central pLL has emerged, the other broad peaks attributed to confined states divide into four smaller peaks under a 50 T real magnetic field. These newly emerged peaks were fitted and found to follow the standard \sqrt{N} single-layer graphene Landau level equation. The exact value of the magnetic field was 50 T, indicating that the splitting of confined states is due to the intrinsic Landau energy level quantization of graphene under a real magnetic field.

Conversely, in the case of a 7 nm high bubble, where pLLs are present, a magnetic field of at least 90 T must be applied to cause peak splitting. This value is comparable to the strength of the PMF [1,27,30].

Interestingly, consistent with the experimental findings by Li *et al.* [14], we see the pLL_{-1} is the only peak that splits. From a theoretical point of view this is due to the electron-hole asymmetry since we consider the next-next-nearest-neighbor hopping in our tight-binding model, which will result in their Fermi velocity having slight differences [14]. The peak splitting transpires due to the emergence of two strain-induced opposing valleys, K_+ and K_- . Upon the introduction of a real magnetic field that is on par with the PMF, an overall effective magnetic field prompts the polarization of the valley and breaks time-reversal symmetry. Consequently, the pLL_{-1} peak bifurcates into two separate peaks, as exemplified in Fig. 1(c) [14,26,27,30]. Another noteworthy characteristic is the central zeroth peaks' independence from the external magnetic field, as depicted in Fig. 1(c). This independence corroborates that all zeroth energy peaks are pLLs, regardless of the bubble height. The underlying reason is the topological protection offered to the zero-energy Landau level [1,28]. Therefore our study implies that the application of an external perpendicular magnetic field offers a viable methodology to differentiate between the strain-induced confined states and pLLs within GNB.

To decipher the differences between confined and pLL states, we examined the site situated at $0.97R$ from the bubble center, representing the three nearest neighbors' hoppings. We defined a function $\delta = \sqrt{\frac{1}{3} \sum_{i=1}^3 (t_i - t_0)^2}$, which depicts its variation with the bubble height. Here, t_0 denotes the nearest hopping without deformation, and t_i corresponds to the nearest hoppings within the bubble. Intriguingly, for a bubble height less than 5 nm, the δ function changes parabolically with the height. Conversely, for a bubble higher than 5 nm, δ linearly increases with height.

As shown in Fig. 2(b), these two tendencies are represented by a blue dashed line and a red dashed line, respectively. These lines intersect at heights of 4.24 and 5.42 nm, reflecting the dynamic evolution of confined and pLL states as the bubble height changes. For heights less than 4.24 nm, the LDOS low-energy part is dominated by confined states ($n \neq 0$). As the height increases from 4.24 to 5.42 nm, the two lines, almost identical, signal the emergence of pLL states near the Fermi level, where pLL states and confined states coexist. For larger bubble heights, the LDOS low-energy part is dominated by the pLLs, and δ grows linearly with bubble height. This growth pattern explains why the PMF's strength linearly increases with the strain level. As we further investigated the physics underlying these dual tendencies, we extracted data on the nearest neighbor hoppings t_i , observing their variation with increasing bubble height. Notably, t_3 , the hopping between the neighbor which is farthest from the bubble center significantly increased, as illustrated in Fig. 2(d). Meanwhile, the hoppings between the other two neighbors displayed a gradual increase correlating with the bubble height. This pattern was particularly pronounced: when the bubble height was less than 3 nm, the hoppings of the two neighbors, t_1 and t_2 , appeared nearly identical. However, as the bubble height exceeded 4 nm, a distinct divergence between t_1 and t_2 emerged.

Concurrently, the disparity between t_3 and t_1, t_2 remained relatively small, and a finite quantum well was formed.

Our findings demonstrate a dynamic evolution of states in a GNB relative to height (or strain). For a small height, the strain profile-generated PMF is insufficient, and the confined states prevail over the pLLs. A slight height increase brings about the appearance of pLLs in the LDOS, resulting in the coexistence of both confined states and pLLs in the system. Once the height is significantly large, the pLLs gain dominance over the confined states. Notably, the LDOS characteristics owe their existence to the bubble's formation, unaffected by substrate interaction, as illustrated by our calculations involving a graphene substrate (see Appendix B).

Understanding local electron movement necessitates knowing the valleys' sign or the strain-induced PMF. This can be determined by extracting the vector potential from our tight-binding model and calculating its curl (see Appendix A). The strain-induced vector field in a paraboloid bubble is shown by arrows in Fig. 2(c), and this field flows in varying directions near the bubble edge. This flow indicates that the LDOS peaks (H-7 nm) are a result of strain-induced PMFs. This explains why the PMF is angle-dependent and only manifests at the strained bubble edge. Collectively, our findings reveal that the PMF identified in experimental results is attributed to electron localization at the paraboloid bubble's edge and electrons behave differently in opposite valleys [9,14,17,19].

An intriguing query pertains to the angle dependence of the PMF along the graphene nanobubbles. As we gently deform the top layer of graphene using the bump function in Eq. (1), if no scattering process occurs between the valleys, the electrons would behave as if time-reversal symmetry is locally broken. However, the effective total flux across the entire sample remains zero. Therefore the valleys K_+ and K_- should be equivalent [19].

III. GAUSSIAN BUBBLE

Gaussian bubbles, which can be induced by applying a voltage to a paraboloid bubble using an AFM or STM tip [9,13], exhibit fascinating features. To shape the bubble, we employ a smooth Gaussian bump function [32]:

$$\delta z = H \exp \left[-\frac{(x - x_0)^2 + (y - y_0)^2}{2\sigma^2} \right]. \quad (5)$$

In this equation, H represents the height of the bubble, and (x_0, y_0) denotes the position at the center of the top layer in the x - y plane. The bubble's radius is given as $R = 3\sigma$, while δz signifies the deformation of the z coordinates.

As evidenced by the strain profile depicted in Fig. 3(b), a PMF is expected to emerge around the middle of the bubble. However, the precise timing of its appearance and its distribution within the bubble, which maintains a fixed radius of 50 nm, remain to be elucidated. To observe the evolution of LDOS with varying bubble height, we selected the site located $0.36 R$ away from the center of the bubble (within the maximum strained region), as marked in Fig. 3(a).

In instances of mild strain, induced pLLs are the only ones detected near the Fermi level. The confined states

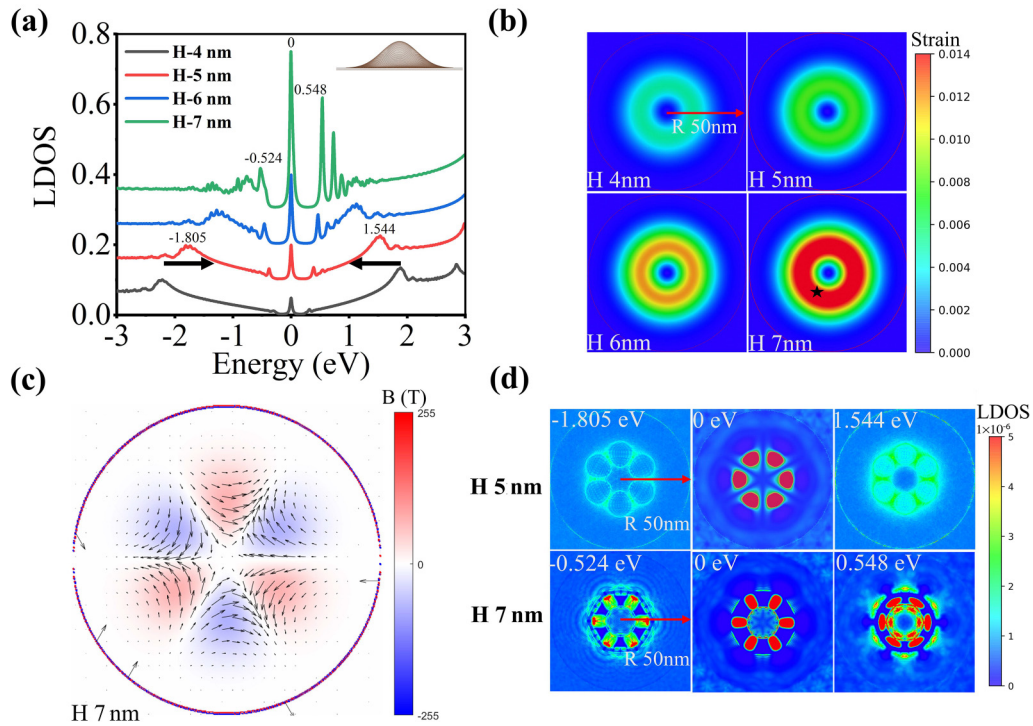


FIG. 3. (a) The site situated at the distance $0.36R$ from the bubble center LDOS evolution with bubble height (they are shifted equally along the y axis for clarity purposes), the black arrows denote the shift tendency in the Gaussian bubble and the side view of a single Gaussian bubble. (b) Strain profiles of the bubble in (a) with different heights, the radius is fixed for 50 nm. (c) The angle-dependent PMF distribution in the single Gaussian bubble with height 7 nm. (d) Quasieigenstates of the LDOS peaks as shown in (a).

predominantly originate closed to van Hove singularities at the high-energy part, as marked in Fig. 3(a). The central zeroth Landau level grows with the bubble's height, while both the first Landau levels on the electron and hole side recede from the Fermi level as the bubble height increases, leading to a boost in the strength of the strain-induced PMF. PLLs appear at a relatively lower strain (around 0.006) compared to the paraboloid cases, a discrepancy we attribute to the variations in the local atomic environment between different bubbles [1].

The δ function fitting outlined in the Appendix E facilitates comprehension of the dynamic evolution of the confined states and pLLs as the bubble height changes. For bubble with the height of 7 nm, the peaks situated near the Fermi level are strain-induced pLLs. The corresponding spatial LDOS for these peaks appears highly similar, indicating an angle-dependent distribution of the PMF around the middle of the Gaussian bubble in Fig. 3(d), while the confined states closed to the van Hove singularities are continuously distributed around the middle of the 5 nm Gaussian bubble.

Our results align with calculations from the vector potential, as seen in Fig. 3(c), and offer explanations for experimental data [9,13]. These findings guide experimentalists aiming to design PMFs of varying locations and strengths by modulating the bubble height with AFM/STM tips [9,13].

IV. TRIANGULAR BUBBLE

The triangular bubble, a typical nanostructure in single-layer graphene, often attracts considerable attention in studies [8,15]. In our research, we modeled a triangular bubble in the

top layer, maintaining a consistent distance of 50 nm between the center and the triangle's three vertices. This is illustrated in Fig. 4(a), and the method to modify the triangular bubble shape can be found in the Appendix D.

The strain profile, as demonstrated in Fig. 4(b), reveals an unstrained region at the bubble's center. This implies that a sufficient degree of strain could engender a strain-induced PMF throughout the entire sample [8,19]. Given this deformed structure, our hypothesis posits that the PMF distribution would intensify at the triangular bubble's midpoint as the height of the bubble increases.

By modulating the bubble's height and targeting a specific site— $0.2R$ from the bubble center which located within the region of maximum strain—we observed an intriguing phenomenon: the coexistence of both confined states and strain-induced pLLs. The dynamic evolution of these states can be comprehended through the application of the δ function (see Appendix E).

As demonstrated in Figs. 4(a) and 4(d), there is a striking similarity in spatial shape, suggesting an angle-dependent distribution of the PMF. The central peaks of zeroth order, which enlarge under strain, are identified as strain-induced pLLs. In the region devoid of strain at the bubble's center, no such states can be detected. This absence of states resembles the spatial distribution of the pLLs ($n = -1, 0, +1$) within the 7 nm bubble. Upon observing the peaks originating from confined states in the 4 nm bubble, we detected some states surrounding the unstrained center ($n = +1$). This could provide a means to distinguish between states induced by PMFs and confined states using STM.

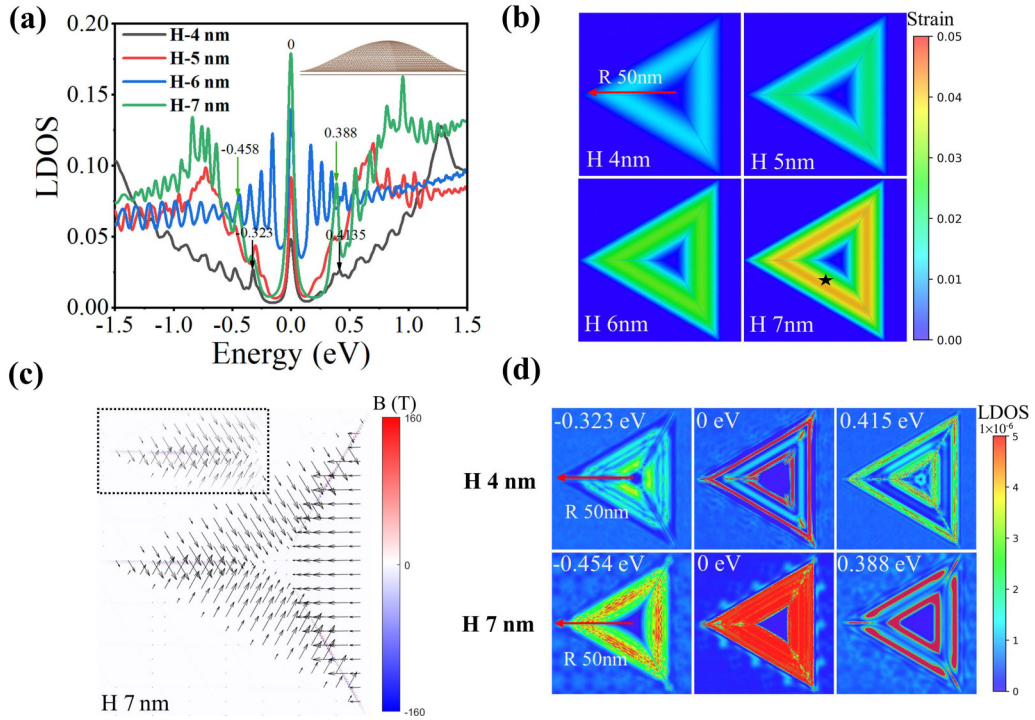


FIG. 4. (a) Illustration of LDOS evolution at site $0.2R$ with varying bubble heights, complemented by a side view of a single triangular bubble. (b) Strain profiles of the bubble depicted in (a) for differing heights, with a fixed distance of 50 nm maintained from the bubble center to each vertex. (c) The angle-dependent PMF distribution in a singular triangular bubble with a height of 7 nm, the black dashed square highlighting a zoom-in of one ridge below. (d) Quasi-eigenstates corresponding to the LDOS peaks shown in (a).

The LDOS fitted PMF (H-7 nm) at the site $0.2R$ from the bubble center approximates 160T, with an energy spacing following the $E \propto \sqrt{N}$ relation. We extracted the vector potential \mathbf{A} and computed the curl of \mathbf{A} , as depicted in Fig. 4(d). Interestingly, the same PMF distribution can be observed in experimental results from one-dimensional ripple structures [14]. Our numerical simulations provide an explanation for the phenomenon of PMF exhibiting different signs between the ripple ridges.

V. CONCLUSIONS

In our investigation, we delved into the electronic properties of three distinct nanobubble shapes in twisted bilayer graphene: paraboloid, Gaussian, and triangular. Employing large-scale numerical simulations and adjusting the bubble heights enabled us to study the strain effects and develop atomic-resolution strain profiles, achieved by extracting the three nearest-neighbor carbon-carbon distances for each atom. Our findings revealed that strain-induced confined states and pLLs coexist universally across all graphene nanobubbles. Notably, under mild strain, the confined states emerge first near the high-energy region, exhibiting a larger peak broadening than the Landau levels and following a linear N spacing rule rather than the conventional \sqrt{N} rule seen in graphene pLLs. As strain intensifies, these confined states migrate to the low-energy region, a shift explainable by the finite quantum well effect induced by a nonuniform PMF. Further increase in strain triggers the appearance of pLLs near the Fermi level, which then expand towards the high-energy region as local strain grows.

According to Figs. 2(b) and 8, and Table I we observed that for confined states and pLLs in three different shapes of graphene nanobubbles, the values of t_1 and t_2 are relatively close. However, t_3 shows a significantly larger deviation from t_1 and t_2 . This observation indicates that the interaction with the third nearest neighbor is more sensitive to variations in bubble height, likely due to its increased distance from the bubble's center. In comparison, the hopping energies for confined states are typically lower than those observed in pLLs. This difference is especially pronounced in the third nearest neighbor hopping t_3 . It implies that confined states are more frequently found in regions of the nanobubbles where the strain is relatively small. This pattern is critical for understanding the distribution and behavior of confined states

TABLE I. Nearest-neighbor hopping energy t_i and the deviation energy ($t_i - t_0$) corresponding to confined states and pLL states, respectively.

Type	Parabolic	Gaussian	Triangle
Confined States			
t_1	-2.961 (+0.24)	-2.868 (+0.33)	-2.928 (+0.27)
t_2	-2.948 (+0.25)	-2.836 (+0.36)	-2.910 (+0.29)
t_3	-2.265 (+0.94)	-1.899 (+1.30)	-2.097 (+1.10)
Pseudo Landau Levels States			
t_1	-2.488 (+0.71)	-2.561 (+0.64)	-2.397 (+0.80)
t_2	-2.450 (+0.75)	-2.500 (+0.70)	-2.340 (+0.86)
t_3	-0.634 (+2.57)	-0.829 (+2.37)	-0.233 (+2.97)

within these strained graphene structures. For confined states, the energy differences between t_3 and t_1 , t_2 are relatively smaller. As a result, electrons maintain the ability to move, leading to a relatively continuous distribution of confined states in graphene nanobubbles. Conversely, when considering pLLs, these differences become significantly larger, resulting in the localization of pLL states in certain regions. Our study provides a comprehensive picture of the dynamic coexistence of confined states and pLLs induced by strain, with the observed strain-induced PMF distribution aligning with previous STM results. We anticipate that the differences between the confined states and Landau levels can be experimentally observed using STM techniques and an external magnetic field. Importantly, our findings not only guide experimentalists in designing spatially-dependent PMFs but also fill a crucial gap in our understanding of strain-induced confined states and PMF states in graphene bubble systems. This research paves the way for future studies on strain-engineered electronic properties in graphene-based systems and the potential development of novel nanoscale devices.

ACKNOWLEDGMENTS

This work was supported by the National Natural Science Foundation of China (Grants No. 12174291 and No. 11974263), and the Natural Science Foundation of Hubei Province, China (2022BAA017). IMDEA Nanociencia acknowledges support from the ‘‘Severo Ochoa’’ Programme for Centres of Excellence in R&D (CEX2020-001039-S / AEI / 10.13039/501100011033). F.G. acknowledges funding from the European Commission, within the Graphene Flagship, Core 3, Grant No. 881603 and from grants NMAT2D (Comunidad de Madrid, Spain), SprQuMat (Ministerio de Ciencia e Innovaci3n, Spain). Z.Z., J.A.S.-G. and F.G. acknowledge support from NOVOMAT, project PID2022-142162NB-I00 funded by MICIU/AEI/10.13039/501100011033 and by FEDER, UE. M.I.K. acknowledges the support by the Dutch Research Council (NWO) via the ‘‘TOPCORE’’ consortium. Z.W. acknowledges the financial support from the China Scholarship Council (CSC). We thank the Core Facility of Wuhan University and the Netherlands National Computing Facilities sponsored by NWO Domain Science for providing the computational resources.

APPENDIX A: NUMERICAL METHODS

In our numerical simulations, the bubbles’ radius are fixed to 50nm, and the hopping parameters $V_{pp\pi}$ and $V_{pp\sigma}$ are described by distance dependent function, since the graphene nanobubble are shaped by smooth bump functions, the strain can be changed continuously by increasing the bubbles’ height without creating or losing extra orbitals. The recursive Green function method implemented codes allow us to handle large-scale samples’ Local Density of States (LDOS) up to millions of atoms precisely. Moreover, the quasieigenstates which reveal the confined states and LLs states spatial distribution can be got and are proved comparable with scanning tunneling microscopy/spectroscopy (STM/S) in the experiments. By extracting the vector potential from our tight-binding model, we can explain the angle-dependent

pseudomagnetic field distribution in the graphene bubble systems, and those results are in good agreement with our spatial LDOS simulation results and published experimental results. The electronic properties of the bubble in twisted bilayer are obtained by using a full tight-binding model based on p_z orbitals. The Hamiltonian of the system has the form [26,33–35]

$$H = \sum_i \epsilon_i |i\rangle \langle i| + \sum_{(i,j)} t_{ij} |i\rangle \langle j|, \quad (\text{A1})$$

where $|i\rangle$ is the p_z orbital located at \mathbf{r}_i , ϵ_i is the on-site energy of orbital i , and $\sum_{(i,j)}$ is the sum over indices i and j with $i \neq j$. The hopping integral t_{ij} , interaction between sites i and j , is

$$t_{ij} = n^2 V_{pp\sigma}(r_{ij}) + (1 - n^2) V_{pp\pi}(r_{ij}). \quad (\text{A2})$$

Here $r_{ij} = |\mathbf{r}_{ij}|$ is the distance between two sites located at \mathbf{r}_i and \mathbf{r}_j , n is the direction cosine of \mathbf{r}_{ij} along the direction \mathbf{e}_z that perpendicular to the graphene layer. The Slater and Koster parameters $V_{pp\sigma}$ and $V_{pp\pi}$ are expressed as distance-dependent functions:

$$\begin{aligned} V_{pp\pi}(r_{ij}) &= -\gamma_0 e^{2.218(b_0 - r_{ij})} F_c(r_{ij}), \\ V_{pp\sigma}(r_{ij}) &= \gamma_1 e^{2.218(h_0 - r_{ij})} F_c(r_{ij}), \end{aligned} \quad (\text{A3})$$

where $b_0 = 1.42 \text{ \AA}$ and $h_0 = 3.35 \text{ \AA}$ represent the nearest carbon-carbon distance and interlayer distance in equilibrium, respectively. The intralayer and interlayer hopping parameters $\gamma_0 = 3.2 \text{ eV}$ and $\gamma_1 = 0.48 \text{ eV}$ are used in all calculations. $F_c(r) = (1 + e^{(r-0.265)/5})^{-1}$ is a smooth function. All the hoppings with $r_{ij} \leq 5.0 \text{ \AA}$ are considered in the calculations. To get the Hamiltonian that describe the nanobubble systems in twisted bilayer graphene, we firstly introduce twisted bilayer graphene without deformation, then reshape the twisted structures by modifying the z coordinates according to smooth bump functions. After deformation, we did not consider lattice relaxation effect in our calculations, which can simulate the bubbles with clamped edges observed in experiments [15]. Since the systems contain around 1.8 million of atoms, it is impossible to get the eigenstates by diagonalization technique. We employ the tight-binding propagation method to calculate the quasieigenstates of the LDOS in graphene nanobubble systems. This method is particularly efficient for handling large systems, as it avoids the need for diagonalization [31]. The time evolution of the $|\Psi(t)\rangle$ can be expressed as

$$|\Psi(t)\rangle = \left[J_0(\hat{t}) \hat{T}_0(\hat{H}) + 2 \sum_{m=1}^{\infty} J_m(\hat{t}) \hat{T}_m(\hat{H}) \right] |\Psi(0)\rangle \quad (\text{A4})$$

where the J_0 and $J_m(\hat{t})$ are the Bessel function of integer order 0 and m , $\hat{T}_m(\hat{H})$ is the Chebyshev polynomial of the first kind, \hat{H} stands for the scaled Hamiltonian, which make its eigenvalues located inside $[-1, 1]$ [31,32]. Firstly, we introduce a random initial state $|\Psi(0)\rangle = \sum_i \alpha_i |\Phi_i\rangle$, which covers a complete set of eigenstates of the system, then the state at time t can be got by expanding the time evolution operator in Chebyshev polynomials, the state at time t has the form $|\Psi(t)\rangle = e^{-iHt} |\Psi(0)\rangle$. By performing the Fourier transformation of $|\Psi(t)\rangle$, the quasieigenstates of the energy E has the

following expression [31,32]:

$$\begin{aligned} |\Psi(E)\rangle &= \frac{1}{2\pi} \int_{-\infty}^{\infty} e^{-iEt} |\Psi(t)\rangle dt \\ &= \frac{1}{2\pi} \sum_i \alpha_i \int_{-\infty}^{\infty} e^{-i(E-E_i)t} |\phi_i\rangle dt \\ &= \sum_i \alpha_i \delta(E - E_i) |\phi_i\rangle \end{aligned} \quad (\text{A5})$$

then the normalized quasieigenstates can be written as

$$|\Psi(\tilde{E})\rangle = \frac{1}{\sqrt{\sum_i |\alpha_i|^2 \delta(E - E_i)}} \sum_i \alpha_i \delta(E - E_i) |\phi_i\rangle. \quad (\text{A6})$$

Here E_i means the eigenvalues of the Hamiltonian, and the superposition of the eigenstates has the same meaning of dI/dV mapping that can be reproduced by the scanning tunneling microscopy experimentally [26,31,36]. The local density of states (LDOS) which describes a space-resolved electron densities of states can be calculated by Green function [26,32]. The LDOS of site i is given by

$$D_i^{\text{LDOS}}(E) = - \lim_{\epsilon \rightarrow 0^+} \frac{1}{\pi} \text{Im} \langle \phi_i | G(E + i\epsilon) | \phi_i \rangle. \quad (\text{A7})$$

Then the diagonal elements of the Green function $G(E)$ are

$$\begin{aligned} G_0(E) &= \langle \phi_0 | G(E) | \phi_0 \rangle \\ &= \frac{1}{E - a_0 - \frac{b_1^2}{E - a_2 - b_2^2 \dots}}. \end{aligned} \quad (\text{A8})$$

The coefficients a_n and b_n in the equation above are defined as [32,37]

$$\begin{aligned} H|\Phi(t_n)\rangle &= a_n |\phi(t_n)\rangle + b_n |\phi(t_{n-1})\rangle + b_{n-1} |\phi(t_{n+1})\rangle, \\ |\phi(t_0)\rangle &= |\phi(0)\rangle, |\phi(t_{-1})\rangle = 0. \end{aligned} \quad (\text{A9})$$

When considering the external perpendicular magnetic field, the hopping terms can be modified according to Peierls substitution:

$$t_{ij} \rightarrow t_{ij} e^{ie \int_i^j \mathbf{A} \cdot d\mathbf{l}} = t_{ij} e^{i(2\pi/\Phi_0) \int_i^j \mathbf{A} \cdot d\mathbf{l}}. \quad (\text{A10})$$

The line integral of the vector potential from site i to j is $\int_i^j \mathbf{A} \cdot d\mathbf{l}$ and $\Phi_0 = ch/e$ is the flux quantum [31,34].

Once we deform the structure, a strain-induced vector field is formed, which is equivalent to adding a real magnetic field. We can extract the vector potential \mathbf{A} from our tight-binding model and it has the form [1,38]

$$A_x = \frac{\sqrt{3}}{2}(t_1 - t_2), A_y = \frac{1}{2}(2t_3 - t_1 - t_2), \quad (\text{A11})$$

where $t_{i=1,2,3}$ are the nearest neighbor hopping terms, once the nonuniform strain is applied, $t_1 \neq t_2 \neq t_3$. The vector potential will create a nonuniform pseudomagnetic field which is proportional to the curl of the vector potential and can be further estimated by [25,39]

$$\mathbf{B} = \frac{c}{ev_f} (\nabla \times \mathbf{A}), \quad (\text{A12})$$

Here, v_f is the Fermi velocity, and c is numerical factor.

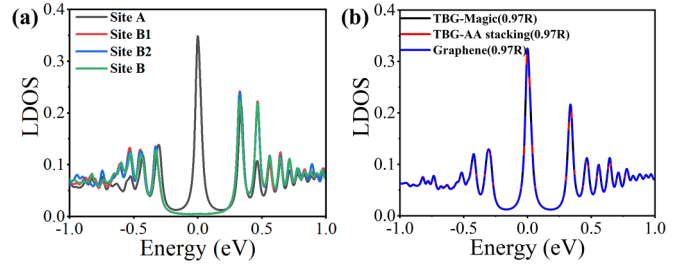


FIG. 5. (a) LDOS for site A and its three nearest neighbors, located $0.97R$ away from the paraboloid bubble center. (b) LDOS comparison for site A at $0.97R$ across magic-angle twisted bilayer graphene (TBG- 1.05°), AA-stacked bilayer graphene (without twist angle), and single-layer graphene paraboloid bubbles.

APPENDIX B: STRAIN-INDUCED SUBLATTICE SYMMETRY BROKEN AND SUBSTRATE EFFECT IN THE GRAPHENE NANOBUBBLES

As illustrated in Fig. 5, the main distinction between site A and its three adjacent atoms is embodied in the central zeroth peak of the LDOS spectrum. Precisely, site A's LDOS showcases this central zeroth peak, while it's conspicuously absent in its neighboring three atoms. In contrast, site B is devoid of a central zeroth peak, but this peak is evident in its three closest neighbors.

This unusual pattern can be traced back to the lattice symmetry disruption provoked by strain. As highlighted in the strain profile in the main body of the text, the strain markedly intensifies near the bubble's edge. Our research discloses that the symmetry-breaking effects triggered by paraboloid deformation parallel those seen when triaxial strain is exerted on a hexagonal graphene flake [40–42].

Turning to Fig. 5, the right panel, we opted for the same site on the paraboloid bubble's edge to study its LDOS under three distinct scenarios: twisted bilayer graphene at the magic angle, AA stacking bilayer, and single-layer graphene. The LDOS at site $0.97R$ away from the bubble center responses are virtually indistinguishable across these different graphene nanobubble systems, suggesting that strain is the primary determinant of the LDOS. Further, the interaction between the graphene's bottom layer and the atoms within the bubble is deemed insignificant due to their considerable separation, thus the substrate effect inside the graphene nanobubbles can be ignored.

APPENDIX C: LDOS COLLECTED ALONG THE LINE APPROACHING TO THE BUBBLE EDGE IN THE SINGLE PARABOLOID BUBBLE

For the single paraboloid bubble, once the bubble radius is fixed for 50 nm, all the LDOS states in the bubble, their low-energy states near the Fermi level are determined by the bubble height. As shown in Fig. 6, when the bubble height is 5 nm, those large broad peaks are confined states, when the bubble height is 7 nm, those sharp peaks correspond to pLLs, for the bubble with height 7 nm, those pLLs almost identical near the bubble edge, which means the pseudomagnetic fields near the bubble edge are almost uniform.

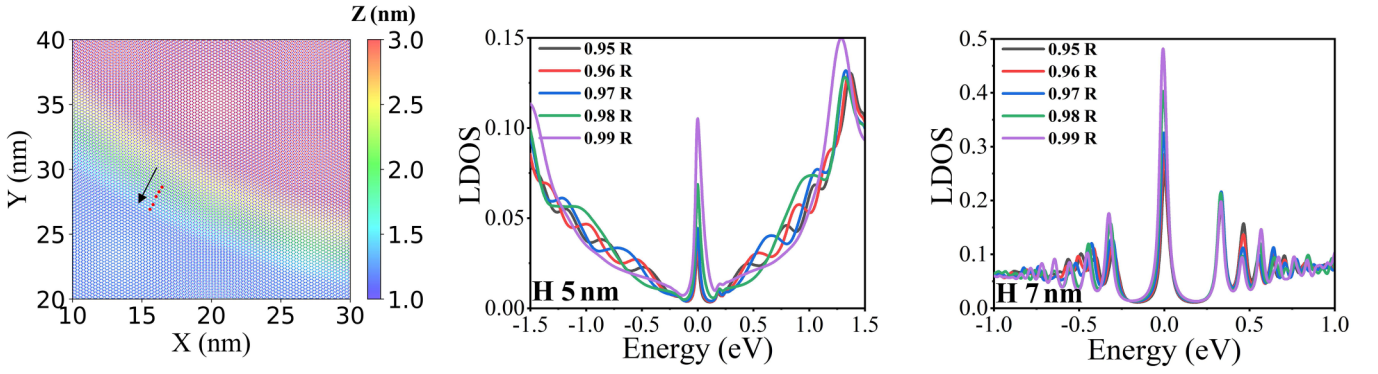


FIG. 6. The points collected along the line at the single paraboloid bubble edge and their LDOS for the height of 5 and 7 nm, respectively.

APPENDIX D: TRIANGULAR BUBBLE CONSTRUCTION METHOD IN TWISTED BILAYER GRAPHENE

The algorithm to construct a triangular bubble in twisted bilayer graphene can be outlined as follows. For a given site S in Fig. 7 (as marked by the star symbol), determine if it resides within the small triangle $\triangle AOB$ through the equation:

$$\vec{OS} = a * \vec{OA} + b * \vec{OB}. \quad (D1)$$

(1) If $a \geq 0$, $b \geq 0$, and $a + b \leq 1$, proceed to adjust the z coordinates in accordance with the smooth bump function:

$$\delta z = H * (\cos(\pi * (a + b)/2))^{1.5}. \quad (D2)$$

In this function, H represents the height of the triangular bubble.

(2) The same algorithm should be applied to sites located within the other two smaller triangles, $\triangle AOC$ and $\triangle BOC$.

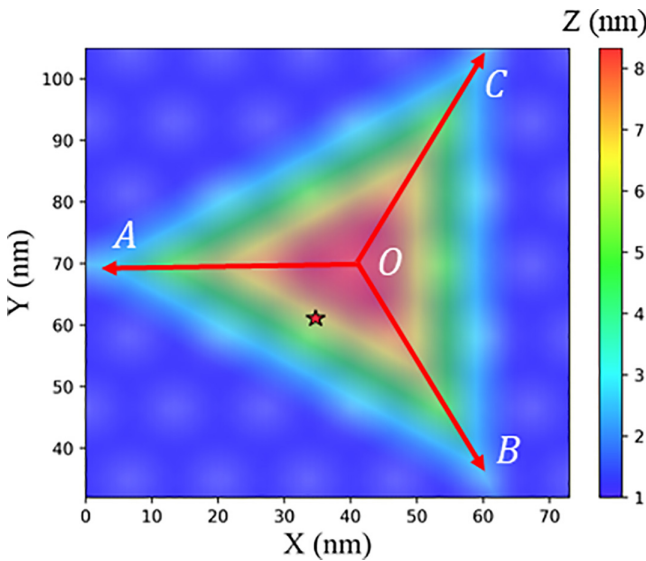


FIG. 7. Top view of a single triangular bubble in twisted bilayer graphene at magic angle 1.05° . The bubble height is 7 nm and \vec{OA} , \vec{OB} , \vec{OC} are 50 nm, O is the triangular bubble center, A, B, C are three different vertices, colorbar stands for the z coordinates of the carbon atoms.

APPENDIX E: DEFINED δ CHANGED AS A FUNCTION OF THE BUBBLE HEIGHT

Figures 8(a) and 8(b) present how the defined function $\delta = \sqrt{\frac{1}{3} \sum_{i=1}^3 (t_i - t_0)^2}$ varies with the height of the bubble, where t_0 signifies the nearest hopping without deformation, and t_i represents the nearest hoppings in the bubble. We discovered that the function δ exhibits the same trend as in a

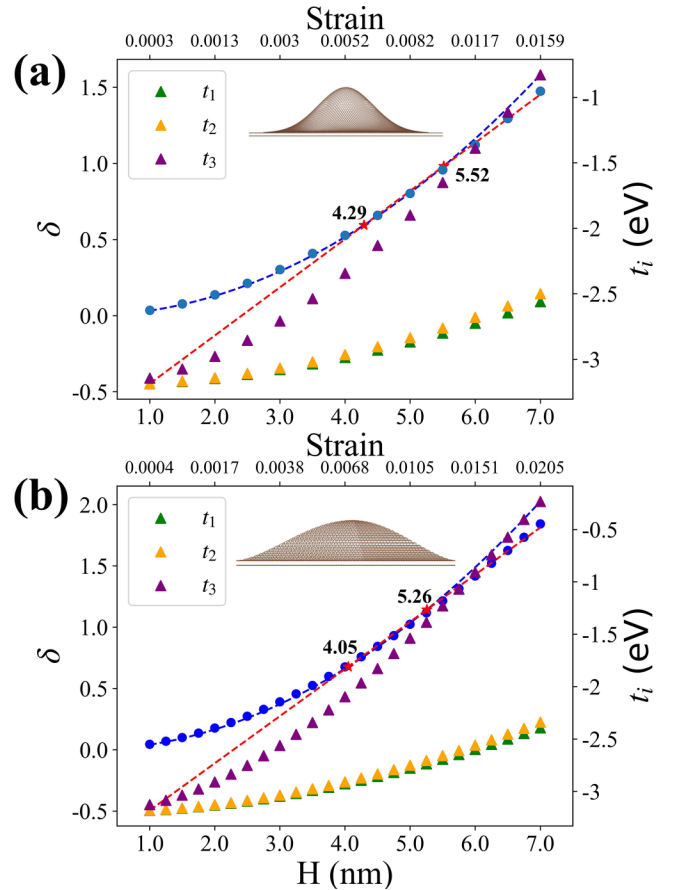


FIG. 8. (a) Variation of the δ function and hopping energies t_i at a site located $0.36R$ away from the center of a single Gaussian bubble, concerning the bubble height. (b) Variation of the δ function and hopping energies t_i at a site located $0.2R$ away from the center of a single triangular bubble, as a function of the bubble height.

single paraboloid bubble when the bubble height is increased. For the Gaussian bubble depicted in Fig. 8(a), confined states emerge around the van Hove singularity when the bubble height is relatively small (less than 4.29 nm). As the bubble height grows, these confined states shift towards the lower energy section, a phenomenon that can also be interpreted through finite quantum well theory. When the bubble height further increases (from 4.29 to 5.52 nm), confined states and Landau Levels (LLs) coexist at the lower energy section (as demonstrated in Fig. 3(a) with a bubble height of 5 nm). Upon further elevation of the bubble height, the LDOS low-energy section is predominantly characterized by LLs (as shown in Fig. 3(a) with a bubble height of 7 nm). Turning to Fig. 8(b), when the triangular bubble height escalates from 4 to 5 nm, the

LLs-like peaks with a substantial broadening shift towards the Fermi level (as shown in Fig. 4(a)). This behavior is consistent with confined state behavior observed in paraboloid and Gaussian bubbles. We attribute these peaks to strain-induced confined states, and this phenomenon can also be explained by the deformation forming a finite quantum well. As the bubble height is further increased, pLLs materialize near the Fermi level, indicating that the pLL states are more localized. When the bubble height is amplified to 7 nm, the pLLs shift towards the higher energy section, suggesting that the pseudomagnetic field grows with the strain [23]. The energy differences between t_3 and t_1 , t_2 also for confined states are relatively lower than pLL states also exist in Gaussian and triangular bubbles.

-
- [1] M. I. Katsnelson, *The Physics of Graphene*, 2nd ed. (Cambridge University Press, UK, 2020).
- [2] K. S. Novoselov, A. K. Geim, S. V. Morozov, D. Jiang, M. I. Katsnelson, I. V. Grigorieva, S. V. Dubonos, and A. A. Firsov, *Nature (London)* **438**, 197 (2005).
- [3] Y. Zhang, Y.-W. Tan, H. L. Stormer, and P. Kim, *Nature (London)* **438**, 201 (2005).
- [4] Y. Cao, V. Fatemi, S. Fang, K. Watanabe, T. Taniguchi, E. Kaxiras, and P. Jarillo-Herrero, *Nature (London)* **556**, 43 (2018).
- [5] Y. Cao, V. Fatemi, A. Demir, S. Fang, S. L. Tomarken, J. Y. Luo, J. D. Sanchez-Yamagishi, K. Watanabe, T. Taniguchi, E. Kaxiras *et al.*, *Nature (London)* **556**, 80 (2018).
- [6] X. Lu, P. Stepanov, W. Yang, M. Xie, M. A. Aamir, I. Das, C. Urgell, K. Watanabe, T. Taniguchi, G. Zhang, A. Bachtold, A. H. MacDonald, and D. K. Efetov, *Nature (London)* **574**, 653 (2019).
- [7] F. Guinea, M. I. Katsnelson, and A. K. Geim, *Nat. Phys.* **6**, 30 (2010).
- [8] N. Levy, S. Burke, K. Meaker, M. Panlasigui, A. Zettl, F. Guinea, A. C. Neto, and M. F. Crommie, *Science* **329**, 544 (2010).
- [9] P. Jia, W. Chen, J. Qiao, M. Zhang, X. Zheng, Z. Xue, R. Liang, C. Tian, L. He, Z. Di *et al.*, *Nat. Commun.* **10**, 3127 (2019).
- [10] C. Yan, Y.-X. Zhao, Y.-W. Liu, and L. He, *Nano Lett.* **23**, 8532 (2023).
- [11] H. Ghorbanfekr-Kalashami, K. Vasu, R. R. Nair, F. M. Peeters, and M. Neek-Amal, *Nat. Commun.* **8**, 15844 (2017).
- [12] M. Settles, S. R. Power, M. Brandbyge, and A.-P. Jauho, *Phys. Rev. Lett.* **117**, 276801 (2016).
- [13] A. Georgi, P. Nemes-Incze, R. Carrillo-Bastos, D. Faria, S. Viola Kusminskiy, D. Zhai, M. Schneider, D. Subramaniam, T. Mashoff, N. M. Freitag *et al.*, *Nano Lett.* **17**, 2240 (2017).
- [14] S.-Y. Li, Y. Su, Y.-N. Ren, and L. He, *Phys. Rev. Lett.* **124**, 106802 (2020).
- [15] E. Khestanova, F. Guinea, L. Fumagalli, A. Geim, and I. Grigorieva, *Nat. Commun.* **7**, 12587 (2016).
- [16] A. V. Tyurnina, D. A. Bandurin, E. Khestanova, V. G. Kravets, M. Koperski, F. Guinea, A. N. Grigorenko, A. K. Geim, and I. V. Grigorieva, *ACS Photonics* **6**, 516 (2019).
- [17] D.-H. Kang, H. Sun, M. Luo, K. Lu, M. Chen, Y. Kim, Y. Jung, X. Gao, S. J. Parluhan, J. Ge *et al.*, *Nat. Commun.* **12**, 5087 (2021).
- [18] W. Yan, W.-Y. He, Z.-D. Chu, M. Liu, L. Meng, R.-F. Dou, Y. Zhang, Z. Liu, J.-C. Nie, and L. He, *Nat. Commun.* **4**, 2159 (2013).
- [19] C.-C. Hsu, M. Teague, J.-Q. Wang, and N.-C. Yeh, *Sci. Adv.* **6**, eaat9488 (2020).
- [20] S. P. Koenig, N. G. Boddeti, M. L. Dunn, and J. S. Bunch, *Nat. Nanotechnol.* **6**, 543 (2011).
- [21] R. Villarreal, P.-C. Lin, F. Faraji, N. Hassani, H. Bana, Z. Zarkua, M. N. Nair, H.-C. Tsai, M. Auge, F. Junge *et al.*, *Nano Lett.* **21**, 8103 (2021).
- [22] N. G. Boddeti, X. Liu, R. Long, J. Xiao, J. S. Bunch, and M. L. Dunn, *Nano Lett.* **13**, 6216 (2013).
- [23] M. Neek-Amal, L. Covaci, K. Shakouri, and F. M. Peeters, *Phys. Rev. B* **88**, 115428 (2013).
- [24] J. Lee, D. Wong, J. V. Jr, J. F. Rodriguez-Nieva, S. Kahn, H.-Z. Tsai, T. Taniguchi, K. Watanabe, A. Zettl, F. Wang, L. S. Levitov, and M. F. Crommie, *Nat. Phys.* **12**, 1032 (2016).
- [25] M. Van Wijk, A. Schuring, M. Katsnelson, and A. Fasolino, *2D Mater.* **2**, 034010 (2015).
- [26] H. Shi, Z. Zhan, Z. Qi, K. Huang, E. v. Veen, J. Á. Silva-Guillén, R. Zhang, P. Li, K. Xie, H. Ji *et al.*, *Nat. Commun.* **11**, 371 (2020).
- [27] Y.-N. Ren, Y.-C. Zhuang, Q.-F. Sun, and L. He, *Phys. Rev. Lett.* **129**, 076802 (2022).
- [28] F. Guinea, M. I. Katsnelson, and M. A. H. Vozmediano, *Phys. Rev. B* **77**, 075422 (2008).
- [29] T. Wehling, A. Balatsky, A. Tselik, M. Katsnelson, and A. Lichtenstein, *EPL (Europhysics Letters)* **84**, 17003 (2008).
- [30] Y.-N. Ren, Q. Cheng, Q.-F. Sun, and L. He, *Phys. Rev. Lett.* **128**, 206805 (2022).
- [31] S. Yuan, H. De Raedt, and M. I. Katsnelson, *Phys. Rev. B* **82**, 115448 (2010).
- [32] Y. Li, Z. Zhan, X. Kuang, Y. Li, and S. Yuan, *Comput. Phys. Commun.* **285**, 108632 (2023).
- [33] G. Yu, Z. Wu, Z. Zhan, M. I. Katsnelson, and S. Yuan, *npj Comput. Mater.* **5**, 122 (2019).
- [34] Z. Wu, Z. Zhan, and S. Yuan, *Sci. China Phys. Mech. Astron.* **64**, 267811 (2021).

- [35] Z. Wu, X. Kuang, Z. Zhan, and S. Yuan, *Phys. Rev. B* **104**, 205104 (2021).
- [36] Y.-W. Liu, Z. Zhan, Z. Wu, C. Yan, S. Yuan, and L. He, *Phys. Rev. Lett.* **129**, 056803 (2022).
- [37] R. Haydock, V. Heine, and M. Kelly, *J. Phys. C* **5**, 2845 (1972).
- [38] M. Long, P. A. Pantaleón, Z. Zhan, F. Guinea, J. Á. Silva-Guillén, and S. Yuan, *npj Comput. Mater.* **8**, 73 (2022).
- [39] M. A. Vozmediano, M. Katsnelson, and F. Guinea, *Phys. Rep.* **496**, 109 (2010).
- [40] S. P. Milovanović, M. Anelković, L. Covaci, and F. M. Peeters, *Phys. Rev. B* **102**, 245427 (2020).
- [41] M. Settnes, S. R. Power, and A.-P. Jauho, *Phys. Rev. B* **93**, 035456 (2016).
- [42] Z. H. Ni, T. Yu, Y. H. Lu, Y. Y. Wang, Y. P. Feng, and Z. X. Shen, *ACS Nano* **2**, 2301 (2008).